Multi-material stainless steel fabrication using plasma wire arc additive manufacturing

Luis Segovia-Guerrero [a], Nuria Baladés [b], Bonnie Attard [c], María De Nicolás [d], Americo Scotti [e], Ann Zammit [c], David L. Sales [d,*]

[a] INNANOMAT Group, Department of Industrial Engineering and Civil Engineering, IMEYMAT, Algeciras School of Engineering and Technology, Universidad de Cádiz, Ramón Puyol Ave, Algeciras, 11202, Spain

[b] IEG Group, Department of Industrial and Civil Engineering, IMEYMAT, Algeciras School of Engineering and Technology, Universidad de Cádiz, Ramón Puyol Ave, Algeciras, 11202, Spain

[c] Department of Metallurgy and Materials Engineering, Faculty of Engineering, University of Malta, Msida, MSD 2080, Malta

[d] INNANOMAT Group, Department of Materials Science and Metallurgical Engineering and Inorganic Chemistry, IMEYMAT, Algeciras School of Engineering and Technology, Universidad de Cádiz, Ramón Puyol Ave, Algeciras, 11202, Spain

[e] Department of Engineering Science, University West, Trollhättan, SE-461 86, Sweden

A R T I C L E   I N F O

A B S T R A C T

Layered stainless steel samples were manufactured using Plasma Wire Arc Additive Manufacturing by depositing alternating layers of two dissimilar stainless steels onto an AISI 316L substrate. The selected materials were the M430 ferritic and M316L austenitic stainless steels. Comprehensive microstructural characterization in different areas, including interfaces between the two different materials, was achieved through optical microscopy and electron backscatter diffraction. Results revealed good weldability among the two-layered steels and on the substrate. Also, a gradient duplex structure was observed mainly at the layer interfaces, suggesting a nuanced blending of properties in the deposited zone. To establish a direct correlation with mechanical properties in the observed structures, macro and micro-hardness tests were conducted along the cross-section. These tests evidenced the presence of a harder phase along the interface compared to the individual materials. The microstructural analysis corroborated the presence of mixing between phases in conjunction with some areas of delta ferrite.

1. Introduction

Stainless Steel (SS) demonstrates remarkable mechanical properties and corrosion resistance overall, rendering it highly applicable in critical sectors; such as chemical processing, aerospace, and the biomedical sector [1,2]. The SS family contains at least 10.5 wt. % (weight percentage) chromium (Cr), less than 1.2 wt% carbon (C) and other alloying elements. Four main categories can be distinguished in the SS family: austenitic, ferritic, martensitic, and duplex. They differ in their present phases, resultant microstructure, composition, properties, and applications.

AISI 316L is an austenitic SS, known for its outstanding corrosion resistance in several industrial and biological environments [3,4]. It is used for medical devices, surgical equipment and structural applications due to its biocompatibility, ease of forming, weldability, and its ability to retain desirable mechanical strength. Furthermore, its remarkably low C content (less than 0.03 wt%) minimizes carbide precipitation, preventing sensitization and subsequent intergranular corrosion when heated, particularly in heat-affected zones from welding processing. In contrast, AISI 430, is a Cr-rich ferritic SS without nickel (Ni). It has good mechanical properties and offers a balance between strength and cost. However, it may not perform as well as austenitic SS in highly corrosive environments. It is used in appliances, kitchenware and architectural components, due to its strength and aesthetic appearance [5,6]. The Duplex SS category, a dual-phase austenite-ferrite alloy, offers excellent mechanical properties and corrosion resistance, especially in aggressive environments. They also have high toughness, fatigue resistance, good weldability, machinability and are magnetic. Emerging grades, like duplex (~22 wt% Cr) and superduplex (~25 wt% Cr) stainless steels, are currently being developed and introduced in the market with enhanced properties [7–10], such as superior corrosion resistance. Therefore, exploring new duplex SS with different compositions is of substantial industrial interest.

Functionally Graded Materials (FGM) are advanced composites with gradual variations in their compositions and structures throughout

* Corresponding author.
   E-mail address: david.sales@uca.es (D.L. Sales).

their volume, giving them unique features and advantages [11–14]. Bimetallic structures are combinations of two different metals with the purpose of obtaining final properties derived from each material. Bimetallic materials offer many advantages over cases where a single material is used. For instance, Rodrigues et al. [15] used a bimetallic structure to achieve a good compromise between cost, weight, and good corrosion properties, substituting Inconel 625 with 316L SS in certain strategic regions of structural components. Wu et al. [12] fabricated a steel-Ni bimetallic component achieving an improvement in mechanical response when subjected to tensile testing, attaining values that surpassed the sum of both materials. It is worth exploring new techniques that can fabricate bimetallic structures and FGM of medium–large format parts to incorporate further functionality within single components in a cost-efficient way.

Additive manufacturing (AM) offers a significant avenue for efficient metal part production, bimetallic structures, and functionally graded materials [11–14,16]. Unlike conventional methods for producing steel components, which involve material removal from a larger piece to achieve the desired shape or structure, AM can reduce manufacturing costs by up to 50% [17]. This is because AM contributes to material savings and shortened fabrication times, aligning with significant process efficiency [18]. Among the AM technologies, Direct Energy Deposition (DED) stands out, which includes Directed Light Fabrication (DLF), Laser Engineered Net Shaping (LENS), Laser Metal Deposition (LMD), 3D Laser Cladding and Wire Arc Additive Manufacturing (WAAM). This study centers on the latter [19], which is a relatively high-deposition-rate technique, facilitating compositional gradients within components.

Within the realm of WAAM technology, arc-based techniques, such as Gas Metal Arc (GMA) and Gas Tungsten Arc (GTA), as well as Plasma Arc (PA), are commonly employed. Different manipulation systems exist for WAAM technology, such as robotic cells and Computer Numerical Control (CNC) gantries [20]. This work employs the PA-WAAM technique, where a constricted arc is generated between a non-consumable tungsten electrode (negative polarity) and the base metal. The W electrode is encased in a special copper (Cu) nozzle (inner chamber) inside the torch, which confines the arc. Inert gas, mainly argon (Ar), is supplied through the Cu inner chamber which is then energized to form a plasma. Shielding gas, also inert, flows out from an outer ring of the special Cu nozzle. Therefore, compared to the more popular GTA-based technique, PA-WAAM offers higher energy density, enhancing arc stability and reducing contamination [19]. This technique is particularly advantageous for performing the deposition of different wires due to the stability of the molten pool and arc, allowing the implementation of various mixtures [21]. It is worth noting that this method imposes no restrictions on the size of the build that can be achieved.

This work seeks to evaluate a novel multilayer component manufactured through additive manufacturing using PA-WAAM. The alternating layers of the component are constructed using austenitic and ferritic stainless-steel wires. Characterization through optical microscopy (OM), scanning electron microscopy (SEM), electron backscatter diffraction (EBSD), and hardness testing over the cross-section will be used to investigate the microstructure and properties of the resulting phases, contributing insights into the potential applications of this bimetallic structure.

2. Materials and methods

This work was conducted using two types of SS wires from Nippon Gases: an austenitic M316L (equivalent to AISI 316LSi) and a ferritic M430 (equivalent to AISI 430). Table 1 shows the composition and mechanical properties, including yield strength (σ_y), ultimate tensile strength (UTS), elongation and Vickers hardness (HV_{10}), of the standardized welding deposition with the 1.2-mm-diameter wires used in

Table 1
Nominal composition (in wt.%) and mechanical properties obtained from standardized deposits using the wires [22,23].

	C [wt.%]	Si [wt.%]	Mn [wt.%]	Cr [wt.%]	Ni [wt.%]	Mo [wt.%]	σ_y [MPa]	TS [MPa]	EL [%]	VH_{10}
M316L	0.02	0.9	1.7	18.5	12	2.7	420	620	35	168
M430	0.05	0.3	0.3	17	–	–	340	540	20	189

Table 2
Operating parameters (where WFS stands for wire feed speed, TS for travel speed, ILCt for interlayer cooling time, SGFR for shielding gas flow rate and PGFR for plasma gas flow rate) for the PA-WAAM process during printing.

| Current (A)	Voltage (V)	WFS (m/min)	TS (mm/min)	ILCt (min)	SGFR (L/min)	PGFR (L/min)
285	22.5	4.4	300	5	12.0	1.2

this study. It should be noted that a very low C content prevents sensitization (chromium carbides precipitation at the grain boundaries), while higher Si contents enhance the pool fluidity, resulting in the formation of flatter and smoother deposited tracks.

The equipment to produce the blocky part via PA-WAAM, is a P1200-4X-I model supplied by ADDILAN (Addilan Fabricación Aditiva S.L., Durango, Spain). This equipment comprises a CNC machine with cartesian axes (gantry). The heat source is a Tetrix 552 AC/DC Synergic Plasma AW GR (SCO 4103) generator and a T drive 4 Rob 3 RE HW, from EWM. Additionally, the machine features a PMW 350-2 torch allowing material deposition with a current of up to 350 A. Since the machine only had one wire feeder, the switching between wires was done manually. The wire spool had to be changed through the wire feeder after the completion of each layer. Throughout the WAAM processing, the voltage was monitored online, to ensure that layers were deposited at a constant torch height (through-the-arc sensor principle). The parametric conditions used for printing these multi-material samples are summarized in Table 2. Argon gas at 99.999% purity (Ar5.0) was used as both plasma and shielding gas.

The studied printed block, schematically shown in Fig. 1, is a square prism with a base measuring 80×80 mm and a height of 16 mm, excluding the substrate, which is a 10 mm-thick AISI 316L machined block with dimensions of 150×150 mm. The multi-material structure was fabricated through PA-WAAM, by depositing six successive layers, each one intercalating the two different welding wires (M316L and M430). The layering sequence was initiated with the M430 wire and concluded with the M316L wire.

The trajectory for the torch's movement, presented visually in Fig. 1(a), was configured as a sequential rectangular zigzag path with a designed bead overlapping of 55%. The trajectory design, influenced by insights gained from previous parametric studies made in the lab, downsizes arc start and stop events, preventing premature and excessive wear of the electrode and minimizing deformations (considering the small dimension of the block). This trajectory strategy has been previously adopted in other investigations, such as in Tenuta et al. [24], and it involves reversing the direction of the trajectory for each successive layer to compensate for the deleterious effects (material and heat accumulation) of the start and end of the plasma arc, specifically, the initial (P_0) and final (P_f) points. This means that each successive layer switches the starting and ending points.

After printing, various test specimens were prepared to suit the metallurgical characterization techniques. For SEM and EBSD, specimens were embedded in bakelite, and metallographically ground using abrasive papers with grit sizes of 180, 240, 600, 800, 1200, and 4000, followed by polishing with diamond suspensions of 3 μm, 1 μm and colloidal SiO_2 oxide polishing suspension (OPS). EBSD analysis was performed using a Carl Zeiss Merlin Field Emission SEM equipped with an EBSD/EDX Ametek detector. The working distance was set between 14 to 16 mm, while the working voltage and the probe current were set to 20 kV and 10 nA respectively, measuring an area of ~0.12 mm².
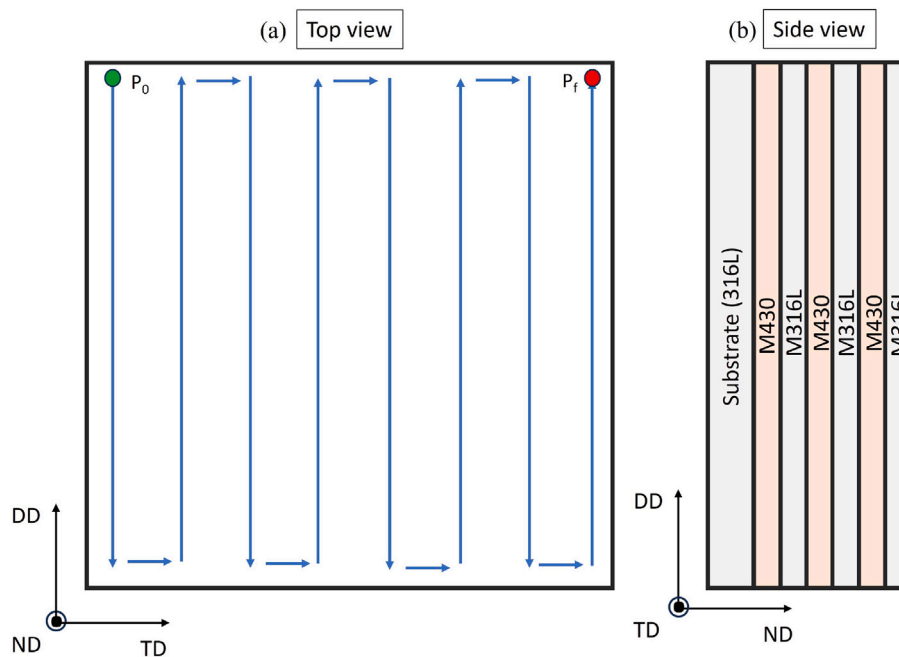
Fig. 1. Trajectory schematic of the multi-material block manufactured by PA-WAAM. The normal (ND), transversal (TD) and deposition (DD) directions are indicated in the reference axes: (a) top view of the trajectory in the DD and TD (blue arrows), where P_0 and P_f represent the starting and ending points; (b) side view of the resultant multi-material along the ND. (For interpretation of the references to color in this figure legend, the reader is referred to the web version of this article.)

OM inspection and hardness tests were conducted on cross-sections of the manufactured samples, which were cut using a cooled disc-cutter, maintaining the faces planar and parallel, followed by metallographically grinding and polishing the specimens. Chemical etching was performed on the OM samples, using a solution of hydrochloric acid, nitric acid and water (*aqua regia*). This etchant was prepared and used according to Table B.8 of Ref. [25]. The etching time was set at 45 s. OM was carried out using a commercial metallographic microscope equipped with a digital camera.

Vickers hardness testing was systematically conducted at multiple locations, equally spaced along an ND-TD plane of the workpiece. Some of the measurements were taken randomly, including at the interfaces between the two different materials. The HV_{10} values were statistically analyzed using commercial statistical software. Micro-hardness $HV_{0.5}$ profiles were obtained along the ND direction with a 250 μm sampling interval, using microhardness equipment.

3. Results and discussion

Fig. 2 shows the macrostructure of the cross-section from the printed multi-material component. No pores or discontinuities were noted along a surface of 2200 mm^2. This emphasizes the robustness of the printed structure, even when different materials are used as sources. Different layers of deposited material are visible, with an average layer thickness of 4 mm. However, this thickness varies depending on the layer material and the position of the weld pass, as observed at different positions within the sample. The substrate is more affected by the first layer dilution in the center than towards the edges, due to the welding heat concentration (the substrate has heat dissipation volume at the blocky part edges [26]). The M430 material penetrates the substrate, and successive beads progressively penetrate the previous bead (the degree of penetration characterizes the dilution). In the studied sample, the first M430 layer penetrated the substrate up to 63%. This maximum degree of penetration was located at the center of the printed part.

Fig. 3 provides a detailed analysis of cross-sectional hardness variation. A boxplot is used to present all the HV_{10} measurements gathered along the ND-DD plane of the multi-material part shown in Fig. 3(a). Results depict values of three distinct areas corresponding to M316L,

M430 and the interface between them. The average HV_{10} hardness of each of them is respectively 183±16, 205±20 and 270±23 HV_{10}, highlighting a statistically significant increase in hardness in the interface zone. Evident fluctuations in hardness values between the two constituent materials are attributed to the inherent disparities between both, M430 and M316L, given the distinct constituent phases of ferrite and austenite, respectively, with dissimilar mechanical properties. The measured hardness was overall higher than that specified by the manufacturer, given in Table 1 for both the constituent alloys considered here. An average difference in the range of 22 units is maintained. The hardness values obtained depend on the cyclic thermal history which can result in relatively high cooling rates leading to a more refined solidification structure together with retained residual stresses [27]. In fact, higher hardness for 316L stainless steel has been documented by Segundo de Lima et al. [28] and the values were comparable to those obtained here using similar travel speed and wire feed speed ranges as were used in this work. Wire feed speed and travel speed will both affect the cooling rate leading to a finer solidification structure (smaller dendrite arm spacing) and a smaller grain size. This tends to offer a higher indentation resistance as per the Hall-Petch relationship [29–31].

Fig. 3(b) provides micro-hardness testing along the cross-section of two beads of different materials. A mean value of 320 $HV_{0.5}$ at the interface was obtained, ranging from 260 $HV_{0.5}$ to 360 $HV_{0.5}$, within the interface region which is much higher than the values obtained in the inner part of the two SS beads. A similar phenomenon has been observed by Saini et al. [32], where the interface between a mild steel and a stainless steel was found to have a statistically significant increase in hardness higher than both parent materials within the interface. The authors attributed this to the formation of a secondary phase based on Cr and C forming at the interface or the occurrence of martensite at this interface. This might also be influenced by the high residual stresses incorporated in the material from rapid cooling, as evidenced by Zhou et al. [5] and Ayan et al. [33] and potential delta ferrite phases inhibiting local deformation [32,34].

To evaluate the predicted changes in the microstructure, OM and EBSD analyses were performed, as shown in Figs. 4 and 5. The micrographs in Fig. 4 show the overall microstructure of different locations,
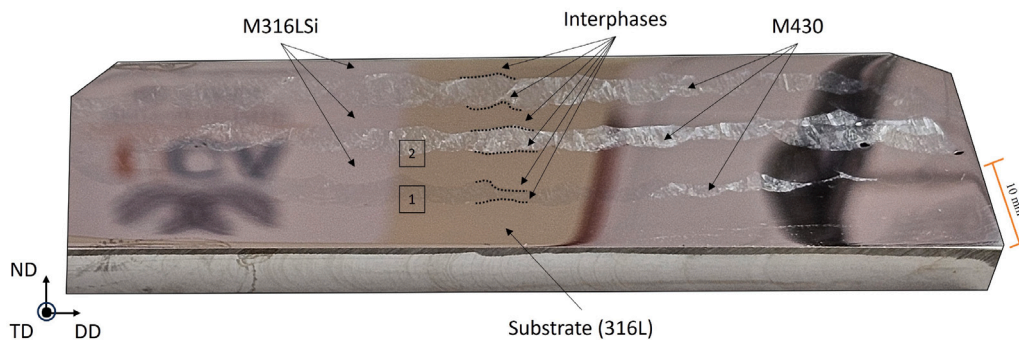
Fig. 2. Cross-section of the original multi-material part (ND-DD direction according to references in Fig. 1) after sanding, polishing, and etching. The alternating layers of materials are clearly visible, with the clear, shiny, darker parts corresponding to M316L, and the lighter whitish ones to M430 as marked. The squares labeled '1' and '2' indicate the studied areas highlighted in Fig. 4. The first layer dilution is visible in the center of the component.
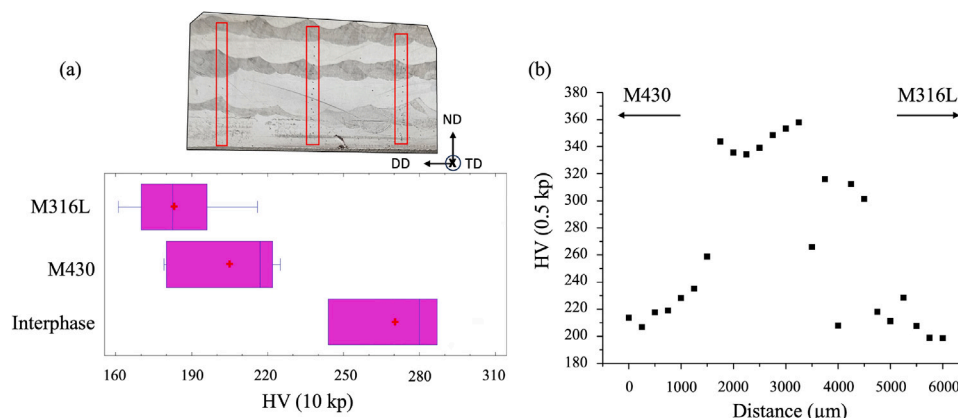
Fig. 3. (a) Box plots of HV_{10} measurements, showing three distinct groups of hardness values within different regions. A picture of the specimen is included at the top of the graph, with red boxes indicating the measurement position. This picture corresponds to the opposite face of the sample shown in Fig. 1. (b) Microhardness profile made in the upper surface of the cross-section cut along the normal direction in the ND-TD plane, through one interface. These measurements also form three groups of $HV_{0.5}$ values, distinct for the M430, M316L and interface sections. (For interpretation of the references to color in this figure legend, the reader is referred to the web version of this article.)

including different interfaces along the DD. A noticeable distinction emerges between the first interface, positioned close to the substrate (Fig. 4(a)), and a subsequent upper interface (Fig. 4(b)). The chemical etching agent has not uniformly affected both interfaces, resulting in discernible optical variations in the exposure of those microstructures. The first M316L-M430 interface appears less affected by the etching process compared to the second one, indicating a higher austenitic content as the etchant selectively highlights the ferritic portion.

To further support our analysis of the predicted changes in microstructure, it is noteworthy to consider the implications of the Schaeffler diagram. This diagram illustrates that when combining two different materials, such as M316L and M430, additional phases beyond those present in the base materials may emerge. Specifically, beyond the expected austenitic phase in M316L and the ferritic phase in M430, the presence of other phases such as delta ferrite and martensite can be anticipated [35]. Notably, what appears to be delta ferrite – which may be responsible for the fluctuation in hardness along the M316L area, as reported by Ayan et al. [13], Saini et al. [32] and Gürol et al. [34] – is evident on both sides of the interface, close to the substrate and only on the 316L side for upper zones. Delta ferrite is susceptible to exhibiting higher hardness values compared to the base material in which it is present. This phenomenon can be attributed to both its composition and crystal structure. Firstly, delta ferrite may possess a higher carbon content than the surrounding material, contributing to increased hardness. Additionally, the BCC crystal structure of delta ferrite typically results in greater hardness compared to the FCC structure of austenite. This disparity in hardness between phases elucidates the observed fluctuation in hardness along the M316L area [35]. The retention of that delta

ferrite could be because of a greater concentration of ferrite-stabilizing elements such as W, Mo, Nb and V [32].

Moreover, there is a 'white band' that appears in the first interface between the two materials, according to Gürol et al. [34], that could be due to an enrichment of carbon. In contrast, the second interface reveals a clearer view of the ferritic structure with columnar grains perpendicular to the welding interface. Conversely, the austenitic component is less distinct.

Fig. 5 shows the EBSD micrographs obtained of the M430-M316L interface. There is a shift in the phase mixture from the side of stainless steel M316L to the side of M430. The mixing zone, or interface, spreads over a distance which varies from 100 μm to 550 μm in the studied area. The grain structure within the interface is characterized by relatively fine ferrite grains for the M430 phase, transitioning to the coarse austenite grains for the M316L phase. Within the interface area, there is a mixing of the austenite phase within the ferrite phase along the deposition direction, together with the mixing of some ferrite within the austenite phase as shown in Fig. 5(a), and in the magnified area shown in Fig. 5(e). This can be attributed to some remelting occurring in between the layers. The ferrite within the austenite phase appears to also form in small quantities at the austenite grain boundaries as shown in a higher resolution in Fig. 5(e). As both alpha and delta ferrite are based on the same crystal structure, this phase could be the delta ferrite observed at the grain boundaries within Fig. 4. Fig. 5(f) shows the estimated austenite content from the austenitic zone to the ferritic zone highlighted in (e). Each value of austenite content shown in this profile has been averaged over a line of 400 μm. The ferrite percentage is complementary to the austenite percentage. In this area of study, the transition from α to γ takes place along ~100 μm. Taking all this
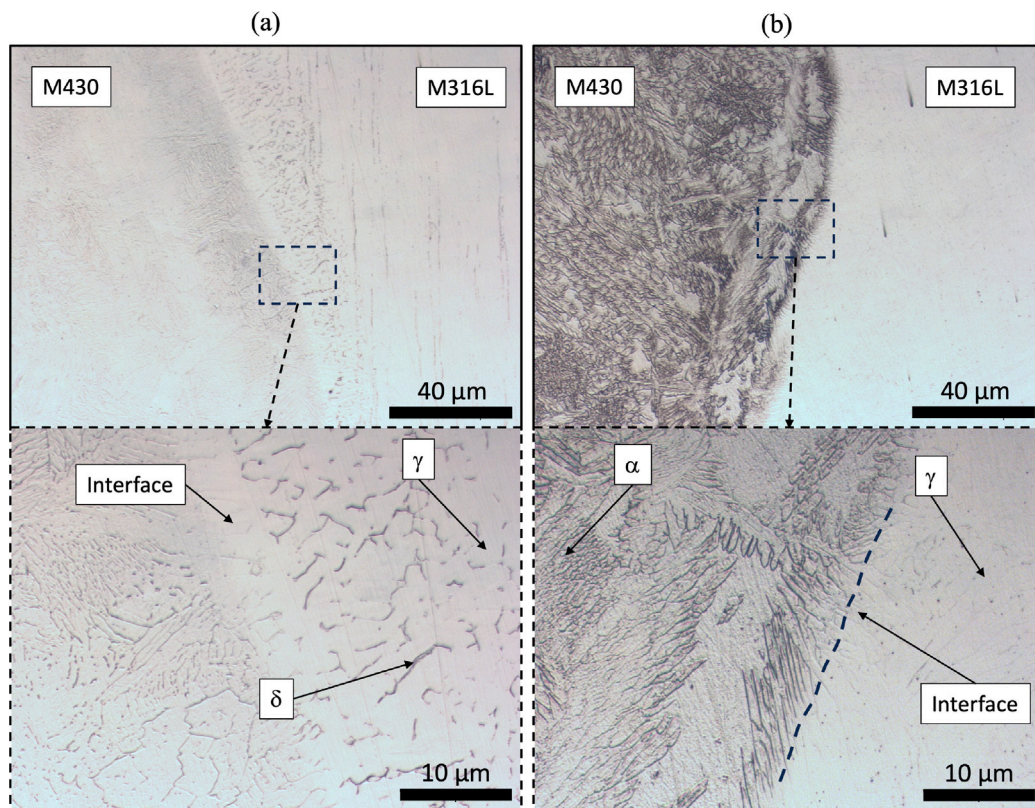
Fig. 4. (a) First interface AISI316 substrate-M430 (see location at point '1' marked in Fig. 2); (b) Second interface M430-M316LSi (see location at point '2' marked in Fig. 2). Two different magnification values are presented.

into account, it can be estimated that 7.5% to 25% of the total volume has a gradient duplex $\alpha - \gamma$ structure, while the rest is formed by a single-phase structure. The image reveals the formation of an interface with a combination of both phases. This suggests a nuanced blending of austenitic and ferritic characteristics in the zone, emphasizing the complexity and interplay of the materials in the vicinity of the interface supporting the relative mixing of phases also observable in Fig. 5(e).

The inverse pole figure map for the interface is shown in Fig. 5(b). The grain structure for the austenite phase consists of large relatively elongated grains with a rotated cube texture along the deposition direction. The ferrite phase consists of relatively large colonies of fine laths growing out of the small grains formed at the interface as shown in the insert in Fig. 5(b).

The kernel average misorientation (KAM) map for the interface and neighboring areas is shown in Fig. 5(c). It is evident that the austenite phase appears to have much lower KAM values overall, indicating a lower amount of geometrically necessary dislocations (GND) within the structure and thus also a reduced resistance to deformation supporting hardness measurements presented in Fig. 3. Some areas within individual grains are highlighted as having high KAM values; possibly indicating residual stresses stored within grains from the WAAM process accounting for the higher hardness compared to what was listed in Table 1. The ferritic phase consists of an area with very high KAM values overall, characterized by small, localized grains where the KAM values are at a maximum indicative of areas with a high density of GNDs resulting in the higher hardness values observed in Fig. 3 for the M430 phase [36,37]. The interface is also characterized by high KAM values while the grain size within the interface region is also very fine, both factors possibly accounting for the increased hardness values obtained within this region. Fig. 5(d) shows the image quality map for the interface region with the coincident site lattices (CSL) overlayed in yellow. The area consisted predominantly of $\Sigma3$ CSL boundaries with a fraction of 0.058 observed in the ferrite phase and a fraction of 0.012

observed in the austenite phase. Coincident site lattice boundaries have been associated with unique mechanical properties due to the low boundary energy affecting the material behavior locally [38].

4. Conclusion

This study investigated the fabrication of a layered multi-material using PA-WAAM technology and two different stainless steels, AISI 316LSi and AISI 430 on an AISI 316L substrate. The employed trajectory, a sequential rectangular zigzag path with a designated overlapping of 55%, along with operation parameters including a current of 285 A, voltage of 22.5 V, wire feed rate of 4.4 m/min, torch traverse speed of 300 mm/min, 5-minute cooling time between layers, a protective gas flow of 12 l/min, and plasma gas flow of 1.2 l/min, have successfully created defect-free multi-material specimens. This process, involving two stainless steels of austenitic and ferritic nature, confirms good weldability between the materials. Visual inspection revealed no visible defects, maintaining consistency with the welding process and showcasing a maximum penetration of 63% at the center of the produced piece, primarily due to heat accumulation during printing.

Hardness examination displayed three distinct zones, corresponding to each material and the interface. Hardness values of 180±16 HV, 205±20 HV, and 270±23 HV were observed for M316L, M430, and the interface, respectively. The multi-material hardness did not fall below the nominal values of the constituent materials, with a region of increased hardness observed near the interface, attributed to finer grain size and a higher degree of geometrically necessary dislocations.

Optical microscopy identified the predominance of gamma austenite in the M316L austenitic stainless steel deposited tracks and alpha ferrite in the M430 ferritic stainless steel deposited tracks. Regions near the interface, particularly in M316L, exhibited delta ferrite, possibly due to the presence of stabilizing elements, explaining the variation in measured hardness.
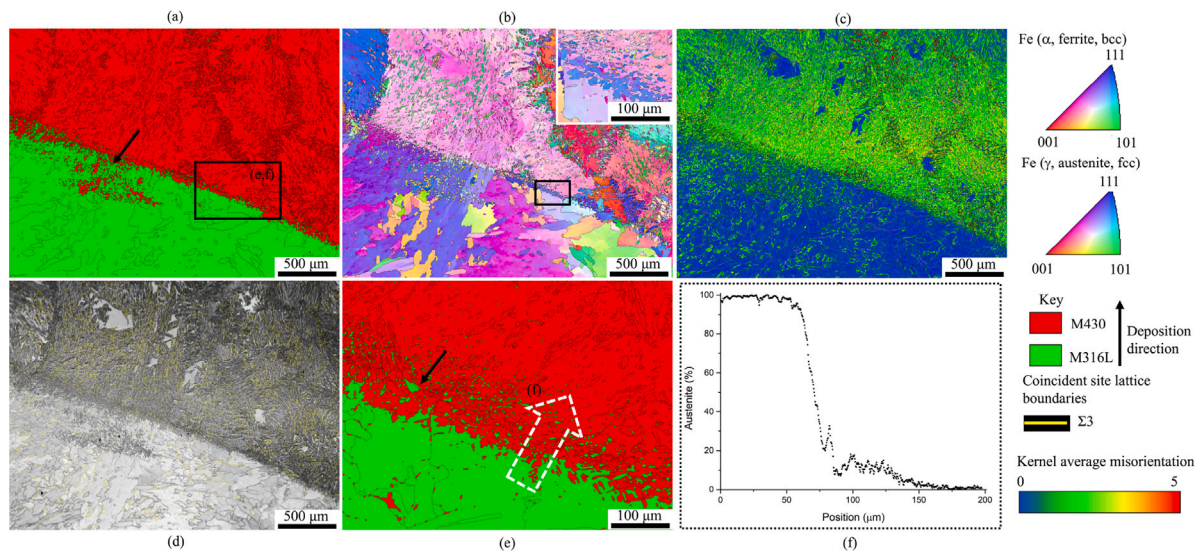
Fig. 5. (a) EBSD Phase Map of the interface close to the upper surface, showing different phases austenitic in green color and ferritic in red color, together with (b) an inverse pole figure map (insert showing the square region marked), (c) a kernel average misorientation map and (d) an image quality map with coincident site lattice boundaries highlighted for the same area, together with (e) a higher resolution of the region marked in (a) and (f) the austenite percentage across the interface measured over the area marked with the dotted white arrow. The black arrows in (a and e) highlight areas of mixing within the interface. The 15 ° grain boundaries are outlined in black on (a, b, c and e). (For interpretation of the references to color in this figure legend, the reader is referred to the web version of this article.)

EBSD analysis revealed several key findings. Firstly, there was a discernible shift in phase mixture from 316L to M430, traversing through the interface, with a length varying between 100 μm to 550 μm. Additionally, M430 exhibited fine ferrite grains transitioning into coarse austenite grains in M316L, accompanied by a continuous transition from austenite to ferrite near the interface. This transition facilitated the formation of a duplex gamma-alpha structure, estimated to occupy 7.5% to 25% of the total volume, imparting unique properties at the interface. The grain structure characteristics depicted relatively large and elongated austenite grains alongside ferrite colonies composed of fine laths emerging from small grains at the interface. Furthermore, the kernel average misorientation analysis unveiled lower values in austenite, suggesting fewer geometrically necessary dislocations, while higher values in ferrite indicated a denser dislocation distribution, which corresponded to observed hardness values. Moreover, the interface region predominantly comprised $\Sigma 3$ coincident site lattice boundaries, with a greater fraction in the ferrite phase, contributing to distinct mechanical properties affecting local material behavior.

These findings suggest that PA-WAAM can be used to create multimaterial stainless steel products with tailored properties and performance for various applications. Furthermore, the study contributes to the understanding of the microstructural evolution and mechanical behavior of Direct Energy Deposition printed multi-material stainless steel components, contributing valuable insights to the field.

Declaration of competing interest

The authors declare that they have no known competing financial interests or personal relationships that could have appeared to influence the work reported in this paper.

References

[1] Feng Y, Zhan B, He J, Wang K. The double-wire feed and plasma arc additive manufacturing process for deposition in Cr-Ni stainless steel. J Mater Process Technol 2018;259:206–15. http://dx.doi.org/10.1016/j.jmatprotec.2018.04.040.

[2] Rizvi SA, Tewari SP. Effect of different welding parameters on the mechanical and microstructural properties of stainless steel 304h welded joints. Int J Eng, Trans A: Basics 2017;30:1592–8. http://dx.doi.org/10.5829/ije.2017.30.10a.21.

[3] Senthil TS, Babu SR, Puviyarasan M. Mechanical, microstructural and fracture studies on inconel 825–SS316L functionally graded wall fabricated by wire arc additive manufacturing. Sci Rep 2023;13. http://dx.doi.org/10.1038/s41598-023-32124-3.

[4] Nagasai BP, Malarvizhi S, Balasubramanian V. Mechanical properties and microstructural characteristics of wire arc additive manufactured 308L stainless steel cylindrical components made by gas metal arc and cold metal transfer arc welding processes. J Mater Process Technol 2022;307:117655. http://dx.doi.org/10.1016/j.jmatprotec.2022.117655.

[5] Zhou J, Shen J, Hu S, Zhao G, Wang Q. Microstructure and mechanical properties of AISI 430 ferritic stainless steel joints fabricated by cold metal transfer welding. Mater Res Express 2019;6. http://dx.doi.org/10.1088/2053-1591/ab4770.

[6] nez AN, Collado I, Almagro JF, Sales DL. Transformation of the microstructure of Fe-Cr steel during its production. Metals 2021;11. http://dx.doi.org/10.3390/met11050806.

[7] Júnior AF, Otubo J, Magnabosco R. Ferrite quantification methodologies for duplex stainless steel. J Aerosp Technol Manag 2016;8:357–62. http://dx.doi.org/10.5028/jatm.v8i3.653.

[8] Hejripour F, Binesh F, Hebel M, Aidun DK. Thermal modeling and characterization of wire arc additive manufactured duplex stainless steel. J Mater Process Technol 2019;272:58–71. http://dx.doi.org/10.1016/j.jmatprotec.2019.05.003.

[9] Baghdadchi A, Hosseini VA, Bermejo MAV, Axelsson B, Harati E, Högström M, et al. Wire laser metal deposition of 22 as-deposited and heat-treated microstructure and mechanical properties. J Mater Sci 2022;57:9556–75. http://dx.doi.org/10.1007/s10853-022-06878-6.

[10] Lervåg M, Sørensen C, Robertstad A, Brønstad BM, Nyhus B, Eriksson M, et al. Additive manufacturing with superduplex stainless steel wire by cmt process. Metals 2020;10. http://dx.doi.org/10.3390/met10020272.

[11] Yoo SW, Lee CM, Kim DH. Effect of functionally graded material (FGM) interlayer in metal additive manufacturing of inconel-stainless bimetallic structure by laser melting deposition (LMD) and wire arc additive manufacturing (WAAM). Materials 2023;16. http://dx.doi.org/10.3390/ma16020535.

[12] Wu B, Qiu Z, Pan Z, Carpenter K, Wang T, Ding D, et al. Enhanced interface strength in steel-nickel bimetallic component fabricated using wire arc additive manufacturing with interweaving deposition strategy. J Mater Sci Technol 2020;52:226–34. http://dx.doi.org/10.1016/j.jmst.2020.04.019.

[13] Ayan Y, Kahraman N. Fabrication and characterization of functionally graded material (FGM) structure containing two dissimilar steels (ER70S-6 and 308LSi) by wire arc additive manufacturing (WAAM). Mater Today Commun 2022;33. http://dx.doi.org/10.1016/j.mtcomm.2022.104457.

[14] Shen C, Pan Z, Cuiuri D, Roberts J, Li H. Fabrication of fe-feal functionally graded material using the wire-arc additive manufacturing process. Metall Mater Trans B: Process Metall Mater Process Sci 2016;47:763–72. http://dx.doi.org/10.1007/s11663-015-0509-5.

[15] Rodrigues TA, Farias FWC, Zhang K, Shamsolhodaei A, Shen J, Zhou N, et al. Wire and arc additive manufacturing of SS316L stainless steel/inconel 625 functionally graded material: Development and characterization. J Mater Res Technol 2022;21:237–51. http://dx.doi.org/10.1016/j.jmrt.2022.08.169.

[16] Li Y, Feng Z, Hao L, Huang L, Xin C, Wang Y, et al. A review on functionally graded materials and structures via additive manufacturing: From multi-scale design to versatile functional properties. Adv Mater Technol 2020;5. http://dx.doi.org/10.1002/admt.201900981.

[17] Vora J, Parmar H, Chaudhari R, Khanna S, Doshi M, Patel V. Experimental investigations on mechanical properties of multi-layered structure fabricated by GMAW-based WAAM of SS316L. J Mater Res Technol 2022;20:2748–57. http://dx.doi.org/10.1016/j.jmrt.2022.08.074.

[18] Zhang C, Yu H, Sun D, Liu W. Fabrication of multi-material components by wire arc additive manufacturing. Coatings 2022;12. http://dx.doi.org/10.3390/coatings12111683.

[19] Martina F, Mehnen J, Williams SW, Colegrove P, Wang F. Investigation of the benefits of plasma deposition for the additive layer manufacture of Ti-6Al-4V. J Mater Process Technol 2012;212:1377–86. http://dx.doi.org/10.1016/j.jmatprotec.2012.02.002.

[20] Singh SR, Khanna P. Wire arc additive manufacturing (WAAM): A new process to shape engineering materials. Mater Today: Proc 2021;44:118–28. http://dx.doi.org/10.1016/j.matpr.2020.08.030.

[21] Reisgen U, Sharma R, Oster L. Plasma multiwire technology with alternating wire feed for tailor-made material properties in wire and arc additive manufacturing. Metals 2019;9. http://dx.doi.org/10.3390/met9070745.

[22] Nippon M-430 product data sheet. 2024, URL https://soldadura.nippongases.com/nippon-m-430.html. (Last Accessed April 2024).

[23] Nippon M-316l product data sheet. 2024, URL https://soldadura.nippongases.com/nippon-m-316l.html. (Last Accessed April 2024).

[24] Tenuta E, Nycz A, Noakes M, Simunovic S, Piro MH. Material properties and mechanical behaviour of functionally graded steel produced by wire-arc additive manufacturing. Addit Manuf 2021;46. http://dx.doi.org/10.1016/j.addma.2021.102175.

[25] for Standardization (Technical Committee: ISO/TC 44/SC 5) EC. ISO/TR 16060:2003 - destructive tests on welds in metallic materials — Etchants for macroscopic and microscopic examination. 2021, p. 1–31, URL https://www.iso.org/standard/29975.html.

[26] Aldalur E, Veiga F, Suárez A, Bilbao J, Lamikiz A. High deposition wire arc additive manufacturing of mild steel: Strategies and heat input effect on microstructure and mechanical properties. J Manuf Process 2020;58:615–26. http://dx.doi.org/10.1016/j.jmapro.2020.08.060.

[27] Kannan AR, Shanmugam NS, Rajkumar V, Vishnukumar M. Insight into the microstructural features and corrosion properties of wire arc additive manufactured super duplex stainless steel (ER2594). Mater Lett 2020;270. http://dx.doi.org/10.1016/j.matlet.2020.127680.

[28] de Lima JS, da Silva Neto JF, Maciel TM, López EAT, de Santana RAC, de Abreu Santos TF. Effect of wire arc additive manufacturing parameters on geometric, hardness, and microstructure of SS316LSi stainless steel preforms. Int J Adv Manuf Technol 2024. http://dx.doi.org/10.1007/s00170-024-13240-4.

[29] Petch N. The cleavage strength of polycrystals. J Iron Steel Inst 1953;174:25–8.

[30] Hall E. The deformation and ageing of mild steel: III discussion of results. Proc Phys Soc Sec B 1951;64:747, URL http://iopscience.iop.org/0370-1301/64/9/303.

[31] Wang L, Xue J, Wang Q. Correlation between arc mode, microstructure, and mechanical properties during wire arc additive manufacturing of SS316L stainless steel. Mater Sci Eng A 2019;751:183–90. http://dx.doi.org/10.1016/j.msea.2019.02.078.

[32] Saini N, Mulik RS, Mahapatra MM, Kannan R, Sharma NK, Li L. Dissolution of δ-ferrite and its effect on mechanical properties of P92 steel welds. Mater Sci Eng A 2020;796. http://dx.doi.org/10.1016/j.msea.2020.139370.

[33] Ayan Y, Kahraman N. Fabrication and fatigue properties of dissimilar steel functionally graded material structure through wire arc additive manufacturing. J Mater Eng Perform 2023. http://dx.doi.org/10.1007/s11665-023-07914-5.

[34] gur Gürol U, Turgut B, Güleçyüz N, Dilibal S, Koçak M. Development of multi-material components via robotic wire arc additive manufacturing. Int J 3D Print Technol Digital Ind 2021;5:721–9. http://dx.doi.org/10.46519/ij3dptdi.1033374.

[35] Mukherjee T, Elmer JW, Wei HL, Lienert TJ, Zhang W, Kou S, et al. Control of grain structure, phases, and defects in additive manufacturing of high-performance metallic components. Prog Mater Sci 2023;138. http://dx.doi.org/10.1016/j.pmatsci.2023.101153.

[36] Gao H, Huang Y. Geometrically necessary dislocation and size-dependent plasticity. Scr Mater 2003;48(2):113–8. http://dx.doi.org/10.1016/S1359-6462(02)00329-9.

[37] Moussa C, Bernacki M, Besnard R, Bozzolo N. About quantitative EBSD analysis of deformation and recovery substructures in pure tantalum. IOP Conf Ser: Mater Sci Eng 2015;89. http://dx.doi.org/10.1088/1757-899X/89/1/012038.

[38] Randle V. The coincidence site lattice and the 'sigma enigma'. Mater Charact 2001;47(5):411–6. http://dx.doi.org/10.1016/S1044-5803(02)00193-6.